RSC Sustainability

ROYAL SOCIETY OF CHEMISTRY

PAPER

View Article Online
View Journal | View Issue

Cite this: *RSC Sustainability*, 2025, **3**, 2619

Deactivation mechanisms of Nb_2O_5 catalyst for esterification of dimethyl adipate: crystal transformation and acid site coking†

Mengyue Li,[a] Yang Li,[b] Bin He,[a] Lijun Han,[a] Ruiyi Yan*[a] and Jiayu Xin *[a]

The deactivation mechanisms of Nb_2O_5 catalysts in fixed-bed reactors were systematically investigated, revealing that carbon deposition and structural phase transformations synergistically drive catalyst degradation. During adiponitrile synthesis, carbon deposits evolve progressively from monocyclic to polycyclic aromatic hydrocarbons, leading to blockage of critical acid sites and reduced catalytic activity. Simultaneously, the phase transformation of Nb_2O_5 to $Nb_{12}O_{29}$ generates oxygen vacancies, which form unsaturated metal coordination sites and alter the catalyst's acidity profile. Regeneration partially reverses this phase transformation, restoring Nb_2O_5 content while reducing $Nb_{12}O_{29}$, thereby improving stability Crucially, maintaining moderate acidity is essential for achieving high nitrile selectivity (>85%) at efficient conversion rates. The study proposes practical strategies to mitigate coke formation and stabilize active sites, including optimized ammonia flow rates and acidic site control. These findings provide a theoretical foundation for enhancing Nb_2O_5 catalyst stability, reducing energy consumption, and extending operational lifespan in industrial nitrile production processes.

Received 21st November 2024
Accepted 15th April 2025

DOI: 10.1039/d4su00731j

rsc.li/rscsus

Sustainability spotlight

This study systematically elucidates the deactivation mechanisms of Nb_2O_5 catalysts in fixed-bed reactors, offering a comprehensive understanding of structural and chemical transformations affecting catalyst performance. By identifying carbon deposition and structural phase transformations as the principal contributors to catalyst deactivation, the research provides actionable insights for improving catalytic stability in industrial adiponitrile production. These findings hold significant implications for reducing waste and energy inefficiencies in industrial chemical processes.

1. Introduction

Adiponitrile (ADN) is a critical intermediate in the production of hexamethylene diamine, which is a key raw material for the manufacture of nylon-66.[1,2] The primary industrial processes for large-scale ADN production rely on butadiene hydrocyanation[3,4] and acrylonitrile electrolytic dimerization,[5,6] both of which are widely adopted due to their high production efficiency and strong industrial scalability. However, despite the high efficiency of these processes, they face significant challenges in terms of sustainability and long-term feasibility, such as the use of toxic reagents, high energy consumption, and catalyst deactivation. For example, the butadiene hydrocyanation process, while having a relatively short reaction pathway (see Fig. 1), requires the use of highly toxic hydrogen cyanide (HCN), which introduces severe safety hazards and operational difficulties.[7] Similarly, although the acrylonitrile electrolytic dimerization process benefits from a broad range of feedstocks and minimal environmental impact,[6] it suffers from high energy consumption and complex reaction conditions, making it less suitable for large-scale industrial application. In contrast, adipic acid amination, while a promising alternative, typically operates at high temperatures (300–350 °C) with boron phosphate as a catalyst. This results in a longer process route, higher production costs, and significant NOx emissions, which contribute to air pollution and exacerbate the greenhouse effect.[8]

In response to these challenges, recent research has focused on developing more environmentally friendly and efficient alternatives. The butadiene reacts with CO and methanol to obtain dimethyl adipate (DMA) followed with direct gas-phase amination of DMA to ADN represents a promising green chemistry-based approach (see in Fig. 1d).[9–13] This method avoids the use of toxic reagents and has the potential for utilizing bio-based feedstocks, thereby reducing the environmental impact of the production process.[14–17] The second direct

[a]*Beijing Key Laboratory of Ionic Liquids Clean Process, CAS Key Laboratory of Green Process and Engineering, State Key Laboratory of Multiphase Complex Systems, Institute of Process Engineering, Innovation Academy for Green Manufacture, CAS, Beijing 100190, P. R. China. E-mail: ryyan@ipe.ac.cn; jyxin@ipe.ac.cn*

[b]*State Key Laboratory of Heavy Oil Processing, College of Chemical Engineering, China University of Petroleum, Beijing 102249, China*

† Electronic supplementary information (ESI) available. See DOI: https://doi.org/10.1039/d4su00731j

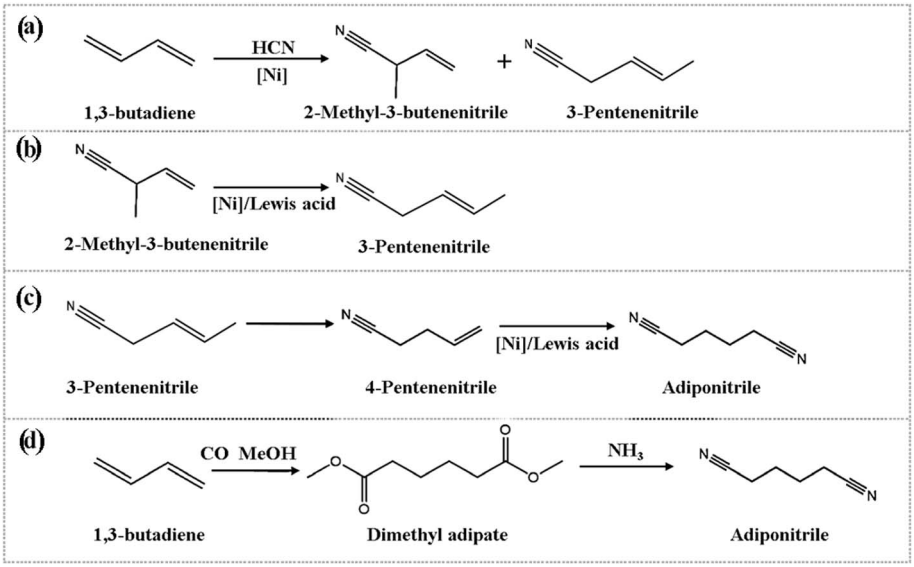

Fig. 1 Cyanidation of butadiene for preparation of adiponitrile.

gas-phase amination reaction is the crucial step for this route.[11,13] Although this method has not yet been extensively studied in academic literature, preliminary studies have shown that the reaction of DMA with ammonia to form ADN is an endothermic process, with a positive reaction enthalpy change (ΔrH) of 42.3 kcal mol^{-1}, indicating that the reaction requires significant energy input, presenting challenges for process optimization.[18] Moreover, a key challenge in this reaction lies in the functionalized carbon chains of DMA and ADN, which contain highly reactive electron-withdrawing groups that may undergo intramolecular cyclization and intermolecular polycondensation, thus affecting reaction selectivity and efficiency.

In this context, acidic metal oxide catalysts, such as Nb_2O_5, V_2O_5, and Ta_2O_5, have demonstrated excellent catalytic activity for the gas-phase conversion of DMA to ADN. Studies have shown that Nb_2O_5 catalysts exhibit high DMA conversion (over 97.7%) and good nitrile selectivity (over 84.3%) in a fixed-bed reactor, making them ideal for this reaction.[18] Compared to other metal oxide catalysts, Nb_2O_5 not only provides excellent conversion but also demonstrates significant advantages in terms of nitrile selectivity. For instance, although Ta_2O_5 shows excellent reactivity, its selectivity towards nitrile products is relatively low, at only 67.8%; V_2O_5 shows similar selectivity to Ta_2O_5 but with a lower DMA conversion.[18] Therefore, Nb_2O_5 catalysts not only offer high conversion but also effectively avoid issues such as equipment corrosion and product separation caused by acidic reactants.[19–21] Nb_2O_5 has shown significant catalytic activity in various reaction systems; however, its stability remains a challenge, particularly under high-temperature conditions. Studies have indicated that the deactivation of Nb_2O_5 catalysts is primarily attributed to sintering, poisoning by non-metal pollutants, and carbon deposition. During high-temperature sintering, Nb_2O_5 particles tend to agglomerate, leading to an increase in particle size, which significantly reduces the specific surface area and catalytic activity of the catalyst.[22,23] Additionally, non-metal pollutants, such as sulfur, nitrogen, phosphorus, and chlorine, react with the catalyst surface to form non-target products. These products can adsorb on the active sites, thereby inhibiting the catalytic reaction rate.[23,24] The impact of these non-target products on the catalyst varies, depending on the type of pollutant and the reaction conditions.[25] In terms of carbon deposition, the carbon source present in the reactants may interact with Nb_2O_5 at elevated temperatures, leading to the formation of solid carbon deposits, which significantly degrade the catalytic performance.[26,27]

Further studies have revealed some unique features of Nb_2O_5 catalyst deactivation in specific reaction systems. For instance, in the ethanol dehydrogenation reaction, the addition of Nb_2O_5 to the ZrO_2–Nb_2O_5 catalyst increased the density of acidic sites.[28] However, an excessive density of acidic sites led to increased ethylene production, which exacerbated the accumulation of carbon sources, thereby impacting catalyst stability. Similarly, in the methane decomposition reaction, when Nb_2O_5 was used as a support for nickel and nickel–copper catalysts, the catalyst surface was found to be completely covered by carbon filaments (CFC), emphasizing the close relationship between carbon deposition at high temperatures and catalyst deactivation.[29] These studies suggest that the deactivation of Nb_2O_5 catalysts is not only related to traditional mechanisms such as sintering and poisoning by non-metal pollutants but also to carbon deposition, which plays a decisive role in catalyst deactivation under specific reaction conditions.

Therefore, the aim of this study is to further explore the performance and deactivation mechanisms of Nb_2O_5 catalysts in gas-phase reactions, and to optimize their performance for large-scale industrial applications by tuning the catalyst's microstructure and adjusting reaction conditions. This research not only provides theoretical guidance for catalyst

design and optimization but also offers valuable insights for the industrial application of DMA to ADN conversion as an environmentally friendly and efficient process.

2. Experimental

2.1 Chemicals and materials

DMA (≥99%) and niobium oxide (Nb_2O_5, 99.9%) were procured from Innochem. Ltd. Ethanol and acetonitrile were sourced from Fuchen Chemical Company (Tianjin, China), and NH_3 was sourced from Beijing YongSheng Gas Technology Co. All reagents utilized in the experiments were of analytical grade.

2.2 Catalyst preparation

Nb_2O_5 was synthesized *via* coprecipitation by first dissolving niobium oxalate in deionized water while stirring at room temperature. Subsequently, the solution's pH was adjusted to 9 using ammonia, resulting in the formation of a solid (Nb_2O_5·H_2O), which was separated *via* filtration. Deionized water was used to wash the solid until the pH became neutral and then dried at 80 °C for 24 h. Finally, Nb_2O_5 was obtained through calcination in a tube furnace.

The aforementioned precursors were positioned flat in a crucible and placed in a tube furnace. Air was supplied to the tube furnace, and the temperature was raised to 700 °C at a rate of 5 °C min^{-1}. The desired sample was calcined at 700 °C for 3 h.

2.3 Equipment and characterization

A Smartlab diffractometer with Cu Kα radiation (40 kV, 150 mA) and a wavelength of 1.5406 Å (Rigaku, Japan) was used to obtain X-ray diffraction (XRD) patterns. The peak resolution error of the XRD data obtained from the Smartlab X-ray diffractometer is controlled within a range of ±0.2°. A micro-TOF II spectrometer with methanol as the mobile phase was used to record electrospray ionization high-resolution mass spectra. A JEM-2100F transmission electron microscope at an accelerating voltage of 200 kV (JEOL, Japan) was used to obtain transmission electron microscopy (TEM) images. SU-8020 scanning electron microscope at an accelerating voltage of 5 kV (Hitachi, Japan) was used to collect scanning electron microscopy (SEM) images. Al as the exciting source (ThermoFisher, USA) was used to perform X-ray photoelectron spectroscopy (XPS) measurements on an ESCALAB 250Xi X-ray photoelectron spectrometer.

A BRUKER Tensor-27 FTIR spectrometer with a DTGS detector was used to perform pyridine adsorption Fourier transform infrared (Py-FTIR) spectroscopy. Each spectrum comprised 32 scans recorded at a resolution of 4 cm^{-1}. Each sample was pressed into a self-supported wafer (20 mg), activated in an evacuated (10^{-3} Pa) chamber at 450 °C for 1 h, and then cooled to room temperature. A background spectrum was also collected. Subsequently, pyridine was introduced into the chamber for 30 min, followed by evacuation for 1 h. The sample was heated at 100 °C, 150 °C and 350 °C for 1 h to assess acid strength, with spectra recorded within the range of 1700–1400 cm^{-1} at room temperature.

2.4 Catalytic tests

A fixed-bed reactor with an internal diameter of 15 mm and a length of 595 mm was used to conduct the nitrile reaction between the monoester and NH_3 (the process flow diagram is shown in Fig. S1†). The reaction airspeed was set at 2.4 h^{-1} (liquid hourly rate of air (LHSV)). 1.5 mL of catalyst (40 mesh) was loaded into the reactor before each experiment, which was then heated to the preheated temperature. A controlled flow rate of NH_3 gas was subsequently introduced into the reactor and measured using a mass flow meter. DMA was introduced into the reactor using a pump after 1 h.

The liquid product was collected by absorption in methanol at 10 °C after a stabilization period of 2 h and subsequently examined offline using an Agilent 4890 gas chromatograph. The column temperature was programmed as follows: initiating at 60 °C for 1 min, followed by a temperature gradient of 25 °C to 225 °C and a final hold of 13 min. The injector and flame ionization detector (FID) temperature were maintained at 250 °C. The following equations were used to calculate the conversion of dimethyl adipate (C_{DMA}) and the selectivity of adiponitrile (S_{ADN}):

$$C_{DMA} = \frac{n_{DMA,inlet}(mol) - n_{DMA,outlet}(mol)}{n_{n_{DMA,inlet}(mol)}} \times 100\% \quad (1)$$

$$S_{ADN} = \frac{n_{ADMA\ transfer}(mol)}{n_{DMA,\ inlet}(mol)} \times 100\% \quad (2)$$

Which $n_{DMA,inlet}$ (mol) represent the feed amount of DMA flowing through the catalyst; $n_{DMA,outlet}$ (mol) represent the feed amount of DMA flowing out the catalyst; $n_{DMA,transfer}$ (mol) represent the DMA of conversion.

In addition to the calibration of the reactor and gas flow rates, we also performed periodic calibration of the mass flow meter used to measure the NH_3 gas, ensuring a measurement error within ±1%. The gas chromatograph (Agilent 4890) was calibrated using standard samples, and its precision was confirmed to be within ±2% for the conversion and selectivity measurements.

3. Results and discussion

In this study, Nb_2O_5 was selected as a model catalyst to evaluate its long-term stability, catalyst deactivation, and regeneration mechanisms in a fixed-bed reactor, as shown in Fig. 2a. Non-precious metal oxides as catalysts demonstrate significant environmental benefits and high atomic efficiency in the synthesis of adiponitrile from dimethyladipate and ammonia, and they exhibit considerable industrial potential.[13,30] During long-term operation tests, the selectivity of the main product and intermediate was not distinguished separately. This is because methyl 5-cyanovalerate (MCP), which is the intermediate, can easily be converted into ADN as demonstrated in our previous research. MCP serves as a key intermediate in the tandem reaction and can be recovered and reintroduced into the reaction system.[18] Therefore, in the simulated industrial operation tests, MCP was treated as a recyclable component and

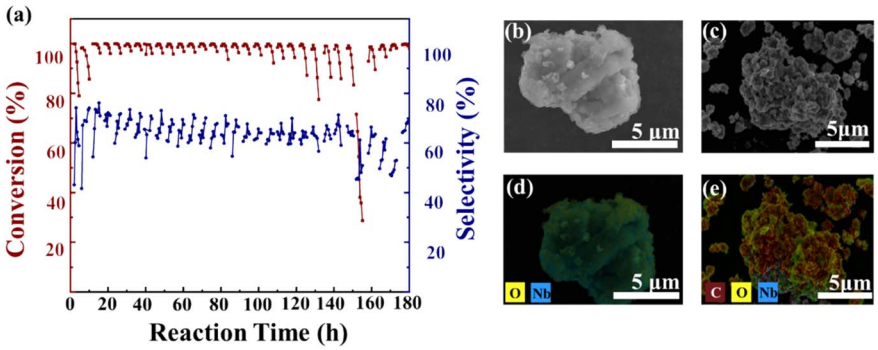

Fig. 2 (a) Catalyst reaction test (T = 375 °C, DMA: 18.3 mmol h^{-1}, NH_3: 4.9 L h^{-1}, NH_3/DMA 12 and LHSV 2.4 h^{-1}); SEM and EDS data of the catalyst before (b and d) and after the reaction (c and e).

was not included in the selectivity calculation. As a result, the selectivity data shown in Fig. 2a reflect the selectivity of the overall products, including the main product and the intermediate.

To ensure the validity of selectivity calculations and the reproducibility of the data, where the main products and by-products were clearly identified. The relevant GC-MS data are provided in the ESI Fig. S2.† The experimental results showed that NH_3/DMA molar ratio of 12, the selectivity of ADN reached 87.6% (Fig. S3†). In this study, Nb_2O_5 was employed as a model catalyst to evaluate its multi-cycle stability in a fixed-bed reactor, as shown in Fig. 2a. During the first 7 h reaction with fresh Nb_2O_5 (F-Nb_2O_5), the conversion dropped from 99.8% to 79%, along with a sharp decline in adiponitrile selectivity. After the reaction, the catalyst (P-Nb_2O_5) appeared blackened carbon deposition, which is a well-known cause of catalyst deactivation.

SEM images (Fig. 2b and c) revealed significant structural collapse of the Nb_2O_5 (P-Nb_2O_5) catalyst surface, indicating that the catalyst framework may have been damaged due to prolonged operation. EDS mapping (Fig. 2d and e) confirmed a significant increase in surface carbon content, suggesting that carbon deposition plays a key role in catalyst deactivation. CHNS elemental analysis (Table S1†) further supported this observation, showing a substantial increase in carbon accumulation on the catalyst surface after the reaction, which may lead to the blockage of active sites, thereby reducing reaction selectivity and conversion. The catalyst lifetime assessment (Fig. 2a) demonstrates that, in addition to performance degradation due to carbon deposition, irreversible deactivation occurs following prolonged operation and repeated regeneration cycles. The crystalline structure of Nb-based catalysts plays a crucial role in determining their physicochemical properties and catalytic activity.[31]

To investigate the structural changes in the deactivated catalyst, X-ray diffraction (XRD) analysis was conducted, and the results are presented in Fig. 3a. The XRD patterns confirm that the primary structure of the catalyst is Nb_2O_5 before the reaction. After the reaction, new diffraction peaks appear at 18.6°, 26.3°, and 30.5°, corresponding to the formation of $Nb_{12}O_{29}$ (JCPDS 19-0863), indicating that the catalytic process induces crystalline modifications in Nb_2O_5.

The phase composition of the catalysts, calculated using the Scherrer equation, is shown in Fig. 3c.[25] After a single reaction (with a test duration of 7 h), the $Nb_{12}O_{29}$ phase content significantly increased. After extending the reaction time to 150 and 180 h, the catalyst's phase composition was predominantly $Nb_{12}O_{29}$. Regeneration experiments conducted after 150 h of reaction (Fig. 3b) show that, despite varying calcination times at 500 °C, the diffraction peak of $Nb_{12}O_{29}$ at 26.3° persists. Even with extended regeneration up to 21 h, the characteristic $Nb_{12}O_{29}$ peak remains unchanged. As shown in Fig. 3d, the calculated content of Nb_2O_5 and $Nb_{12}O_{29}$ across different catalysts indicates that after 21 h of regeneration, the Nb_2O_5 content does not increase with prolonged calcination, and the $Nb_{12}O_{29}$ content shows no significant variation. These observations suggest that the deactivation of Nb_2O_5 catalysts is not solely due to carbon deposition but also involves significant alterations in the catalyst's surface structure. To fully elucidate the deactivation mechanism, further analysis is required to quantify the individual and combined effects of carbon deposition and structural changes within the catalyst.

In this study, we analyzed carbon deposits from two locations: inside the fixed-bed reactor (Carbon-F) and on the catalyst surface (Carbon-C). Thermogravimetric Analysis (TGA) identified the coke species, as shown in Fig. S4.† Most carbon deposits, whether in the reactor or on the catalyst, consisted of hard, aromatic compounds, removable at 550 °C. We used Liquid Chromatography-Mass Spectrometry (LC-MS) to qualitatively analyze these coke species, confirming their types and pathways of accumulation.[32–35] The identified carbon species ranged from aliphatic hydrocarbons and olefins to single-ring and fused-ring aromatic hydrocarbons, as well as amorphous and graphitic carbon.

Prior to LC-MS analysis, the carbon deposits on the catalyst were dissolved, with their solubility classified by their ability to dissolve in specific solvents.[36,37] We employed the Guisnet method,[38] where carbon deposits from the reactor (Carbon-F) and the post-reaction catalyst were treated with hydrofluoric acid to degrade the catalyst. Dichloromethane, an organic solvent, was used to extract soluble carbon, while insoluble carbon was separated by centrifugation. The LC-MS analysis of the dichloromethane extract differentiated the soluble carbon

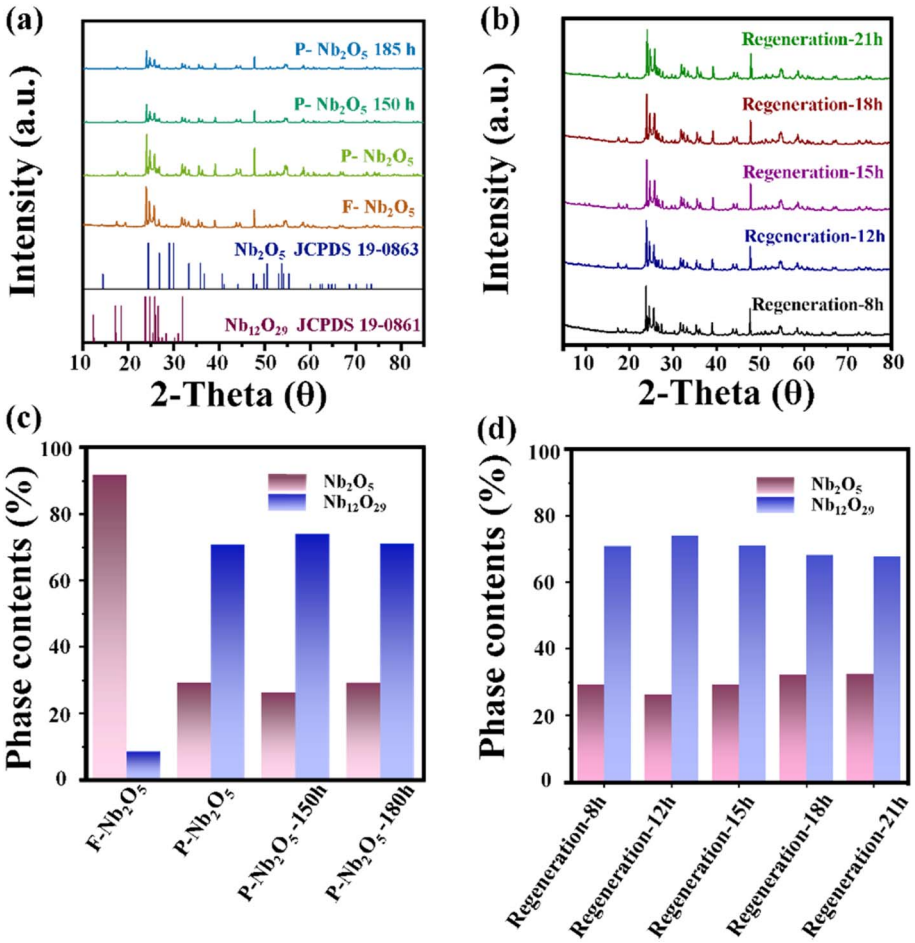

Fig. 3 X-ray diffraction (XRD) patterns and phase content of F-Nb_2O_5, P-Nb_2O_5 and various catalysts to different reaction times (a and c); the XRD patterns and phase content of catalysts regenerated at 550 °C in an air atmosphere for varying durations (b and d).

species, unaffected by inorganic acids.[39] LC-MS chromatograms for Carbon-F and Carbon-C identified the main species, listed in Table 1. Carbon-F was primarily composed of malonic dihydrazide, with small amounts of pentanenitrile, likely due to ammonolysis and hydrolysis during the reaction.[40] Myo-inositol was the major component of the soluble carbon deposits on the

Table 1 Main components of soluble carbon

	Name	Formula	#CAS
Carbon-C			
	Methanol	CH_4O	67-56-1
	Hydrazine	H_4N_2	302-01-2
	Oxalyl dihydrazide	$C_2H_6N_4O_2$	996-98-5
	1,2-Diformylhydrazine	$C_2H_4N_2O_2$	628-36-4
	Malonic dihydrazide	$C_3H_8N_4O_2$	3815-86-9
	N,*N*″-Methyleneis-urea	$C_3H_8N_4O_2$	13547-17-6
	Hexanedioyl azide	$C_6H_8N_6O_2$	25021-15-2
	Pentanenitrile	C_3H_7NO	33279-01-5
	Myo-inositol	$C_6H_{12}O_6$	87-89-8
Carbon-F			
	2,5-Dimethyl-3,4-hexanediol	$C_8H_{18}O_2$	22067-11-0
	2,2-Dimethoxypropane	$C_5H_{12}O_2$	77-76-9
	2,3-Diazabicyclo [2.2.1]hept-2-yl,3-(1,1-imethylethyl) – (9CI)	$C_9H_{17}N_2$	40953-67-1
	Propionamide	C_3H_7NO	79-05-0
	N-Methylacetamide	C_3H_7NO	79-16-3

catalyst, possibly formed through cyclization during the reaction.

Myo-inositol is identified as the primary component of Carbon-C, likely due to its formation during the reaction process. In catalytic reactions, especially those involving hydrocarbons, complex chemical transformations such as cyclization, polymerization, and condensation can occur.[41,42] Myo-inositol, being a relatively stable cyclic compound, is more likely to persist under the reaction conditions and subsequently be detected in the soluble fraction of the carbon deposits.

During dichloromethane extraction, a black precipitate, termed "insoluble carbon", was separated by centrifugation. This hydrocarbon, with a molecular weight exceeding that of pyrene,[43,44] was identified as primarily amorphous carbon *via* X-ray diffraction (XRD) analysis (Fig. S5a†). Raman spectroscopy revealed G (1580–1600 cm^{-1}) and D (1360–1400 cm^{-1}) peaks (Fig. S5b†), indicating a disordered carbon structure with low graphitization, as shown by an I_D/I_G ratio of 1.88.[40,45] Transmission electron microscopy (TEM) images (Fig. S5c and d†) further confirmed a block-like structure.

To monitor changes in carbon species during the nitridation reaction, the Nb_2O_5 catalyst was analyzed at different time intervals (3, 5, 10, and 25 h), with samples collected at distinct deactivation stages, labeled as Nb_2O_5 (3), Nb_2O_5 (5), Nb_2O_5 (10), and Nb_2O_5 (25). FT-IR spectroscopy was used to examine the vibrations of functional groups on the catalysts over time, as shown in Fig. 4a. Carbon deposition is typically observed between 1300 and 1800 cm^{-1}, while the C–H vibration region appears at 2600–3200 cm^{-1}. Peaks at 1460 and 1620 cm^{-1} correspond to fused-ring and single-ring aromatic hydrocarbons, respectively.[40,46–48] The increasing intensities of these peaks indicate that aromatic hydrocarbons are the primary components of carbon deposition. Peaks between 1360 and 1460 cm^{-1} are associated with both aliphatic and aromatic hydrocarbons.[49–51] The decreasing intensity of the aliphatic hydrocarbon peak at 1390 cm^{-1} and the increasing intensity of the aromatic hydrocarbon peak at 1460 cm^{-1} suggest that polycyclic aromatic hydrocarbons become the main constituents of carbon deposition over time. In the C–H vibration region (Fig. 4b), peaks at 2960, 2920, 2870, and 2830 cm^{-1} correspond to CH_2 and CH_3 groups,[52,53] with their increasing intensities indicating a rise in aliphatic hydrocarbon content as the reaction progresses. LC-MS data (Table 1) further show that the soluble carbon species in the deposits shift from single-ring aromatic hydrocarbons to condensed-ring aromatic hydrocarbons as reaction time increases (Fig. 4c).

The impact of carbon build-up on the catalyst pore structure and its effect on catalytic performance can be thoroughly assessed through nitrogen adsorption and desorption analysis. As depicted in Fig. 5a, the nitrogen adsorption isotherms reveal a marked decrease in both microporous and total adsorption with increasing reaction time at low relative pressures (P/P_0). This trend suggests that as the reaction progresses, surface micropores become increasingly obstructed by carbon deposits, thereby limiting the interaction between active sites and the reactants. To further explore the extent of carbon deposition, X-ray photoelectron spectroscopy (XPS) was employed to quantify the surface carbon content. Fig. 5b presents the XPS-derived C/Nb molar ratio for samples subjected to different reaction durations. The C/Nb ratio was calculated using eqn (3)

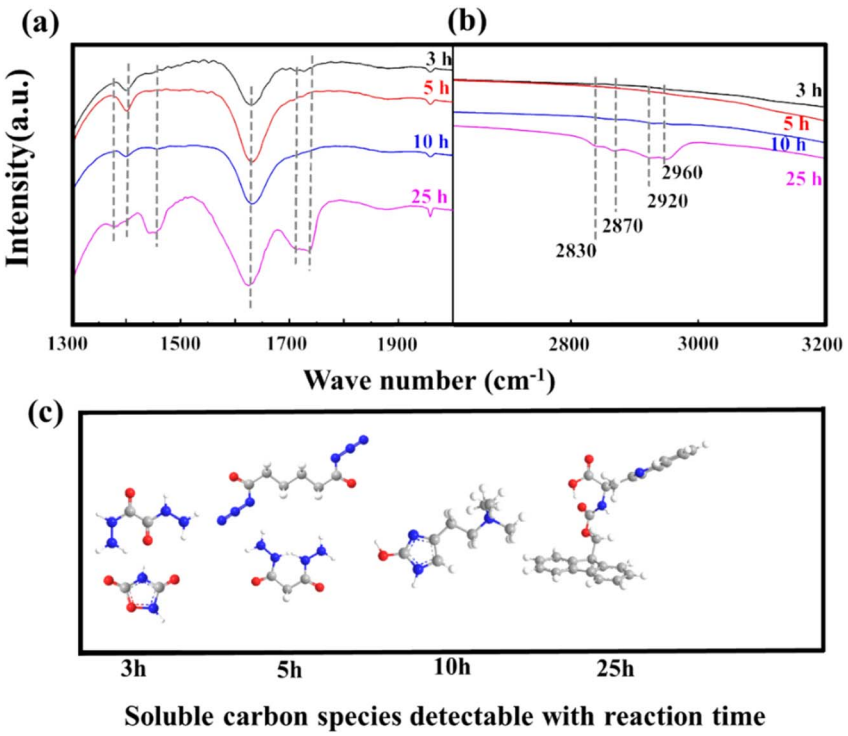

Fig. 4 (a and b) FT-IR spectroscopy and (c) soluble carbon species detectable with reaction time on Carbon-C.

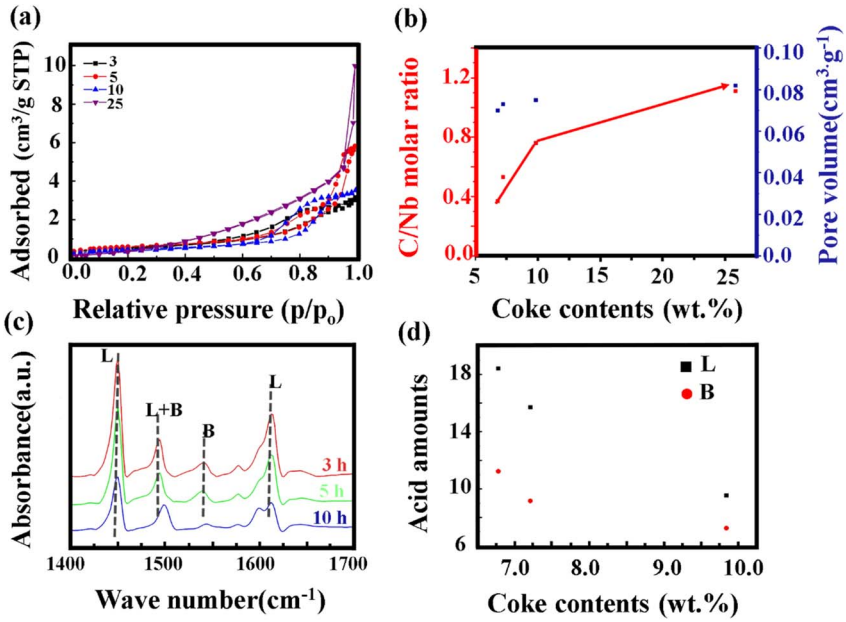

Fig. 5 (a) Nitrogen adsorption and desorption isotherms of catalysts after various reaction times; (b) measured C/Nb ratios by XPS (red) and micropore volume (blue) of various samles as a function of coke weight content; (c) Py-IR spectra of catalysts after different reaction times; (d) peak area of the bands at 1450 and 1540 cm^{-1} *versus* coke content similarities (b and c).

$$\frac{C}{Nb} = \frac{I(C\ 1s)}{I(Nb\ 3d)} \times \frac{\sigma(Nb\ 3d)}{\sigma(C\ 1s)} \quad (3)$$

where $\sigma(C\ 1s) = 1.0$ and $\sigma(Nb\ 3d) = 0.817$.[54] The results show a clear increase in the C/Nb ratio with extended reaction times, indicating that carbon predominantly accumulates on the outer surface of the Nb_2O_5. The lack of significant change in micropore volume, despite the rise in carbon content, reinforces the conclusion that carbon deposition is primarily an external phenomenon. The previous analysis confirms that carbon build-up occurs mainly on the outer surface, which is consistent with the hypothesis that carbon deposition obstructs the catalyst's acid sites, critical for nitrile hydrogenation.[4] To further elucidate, infrared spectroscopy was conducted to examine the acid sites at different stages of the reaction, with the findings presented in Fig. 5c. The spectra show a significant reduction in the peak intensities corresponding to the L (1450 cm^{-1}) and B (1540 cm^{-1}) acid sites as reaction time increases, signaling that these sites are progressively masked by carbon deposits.

Integration of the spectral data, as depicted in Fig. 5d, quantifies the impact of carbon accumulation on these acid sites. The integrated peak area for the L acid site shows a substantial decline with increasing carbon content, while the B acid exhibits a less pronounced reduction. This suggests that carbon deposition predominantly targets the L acid, impairing their functionality. Consequently, the reduction in available acid sites due to carbon deposition hinders the diffusion of reactants and products, thereby contributing to catalyst deactivation over time. This comprehensive analysis underscores the dual impact of carbon deposition: blocking of micropores and masking of crucial acid sites, both of which play pivotal roles in the observed catalyst deactivation. Further studies are required to explore mitigation strategies and optimize catalyst design for improved resistance to carbon-induced deactivation.

These findings indicate that carbon deposition plays a crucial role in blocking micropores and masking acid sites, leading to a gradual decline in catalytic performance. However, to fully elucidate the mechanisms of catalyst deactivation, it is essential not only to explore the impact of carbon accumulation but also to investigate the structural changes occurring within the Nb_2O_5 catalyst itself during the reaction.[55,56] By examining the crystallographic phase transitions and surface structural modifications that occur under reaction conditions, we aim to gain a deeper understanding of the relationship between catalyst structure and its long-term stability.

The valence states of F-Nb_2O_5 and P-Nb_2O_5 were analyzed using XPS, as shown in Fig. 6a and b. For P-Nb_2O_5, the Nb 3d peaks were observed at 205.6 and 208.3 eV, corresponding to Nb $3d_3/_2$ and Nb $3d_5/_2$, respectively, which are characteristic of Nb^{5+} in Nb_2O_5.[57,58] Additionally, companion peaks at 204.9 and 207.8 eV, associated with Nb^{4+}, were also identified.[59,60] These results suggest that during the reaction, a portion of Nb^{5+} was reduced to Nb^{4+}, which aligns with the presence of $Nb_{12}O_{29}$ observed in the XRD analysis. Given these observations, it is crucial to further investigate how the reaction conditions, particularly the ammonia atmosphere and temperature, influence these structural changes in the catalyst. In the subsequent experiments, we will focus on examining the evolution of the catalyst structure under varying ammonia concentrations and thermal conditions, aiming to better understand the factors driving the reduction of Nb^{5+} to Nb^{4+}.

As illustrated in Fig. 7a and b, the XRD patterns reveal the impact of different reaction temperatures and durations on the crystalline structure of Nb_2O_5. The experiments were conducted

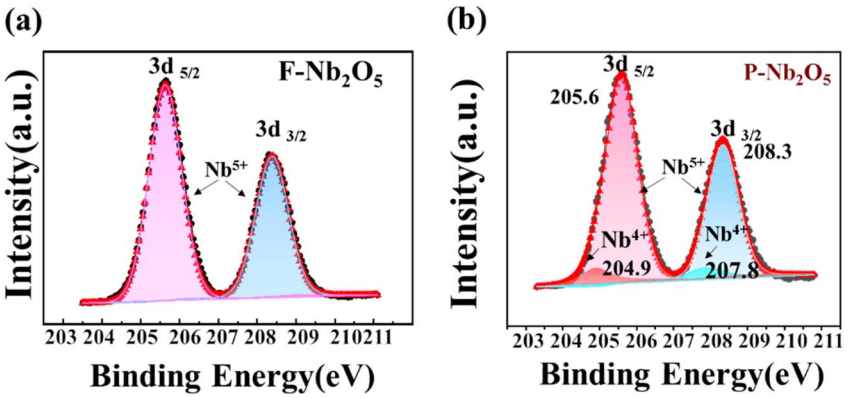

Fig. 6 XPS patterns of Nb 3d (a and b) of the catalyst before and after the reaction.

using a Cu Kα radiation source ($\lambda = 1.5406$ Å) with a scanning range of 10°–80°, a step size of 0.02°, and a scanning rate of 2° min^{-1}. As the reaction temperature increases or the duration extends, the diffraction peaks become sharper and more defined, indicating enhanced crystallinity. However, the peak positions remain consistent with Nb_2O_5 (JCPDS 19-0861), confirming its structural stability under the investigated conditions. This suggests that while higher temperatures or longer reaction times facilitate crystallization, they do not induce a phase transition within the tested parameter range.

Further insights into the oxidation state of niobium under varying reaction conditions were obtained from XPS analysis (Fig. 7d and e). Across the temperature range of 200 to 500 °C and reaction times spanning 2 to 10 h, the Nb^{5+} peaks exhibit clear separation without significant shifts, indicating that niobium predominantly retains its Nb^{5+} oxidation state. This finding substantiates that temperature and reaction time alone do not contribute to the reduction of Nb^{5+}.

In the NH_3 reduction experiments, the XRD patterns under different NH_3 flow rates (Fig. 7c) indicate that as the NH_3 flow rate increases from 2.0 ml min^{-1} to 6.0 ml min^{-1}, new diffraction peaks emerge at 18.6°, 26.3°, and 30.5°, corresponding to $Nb_{12}O_{29}$ (JCPDS 19-0863). This confirms a gradual phase transition from Nb_2O_5 to $Nb_{12}O_{29}$ with increasing NH_3

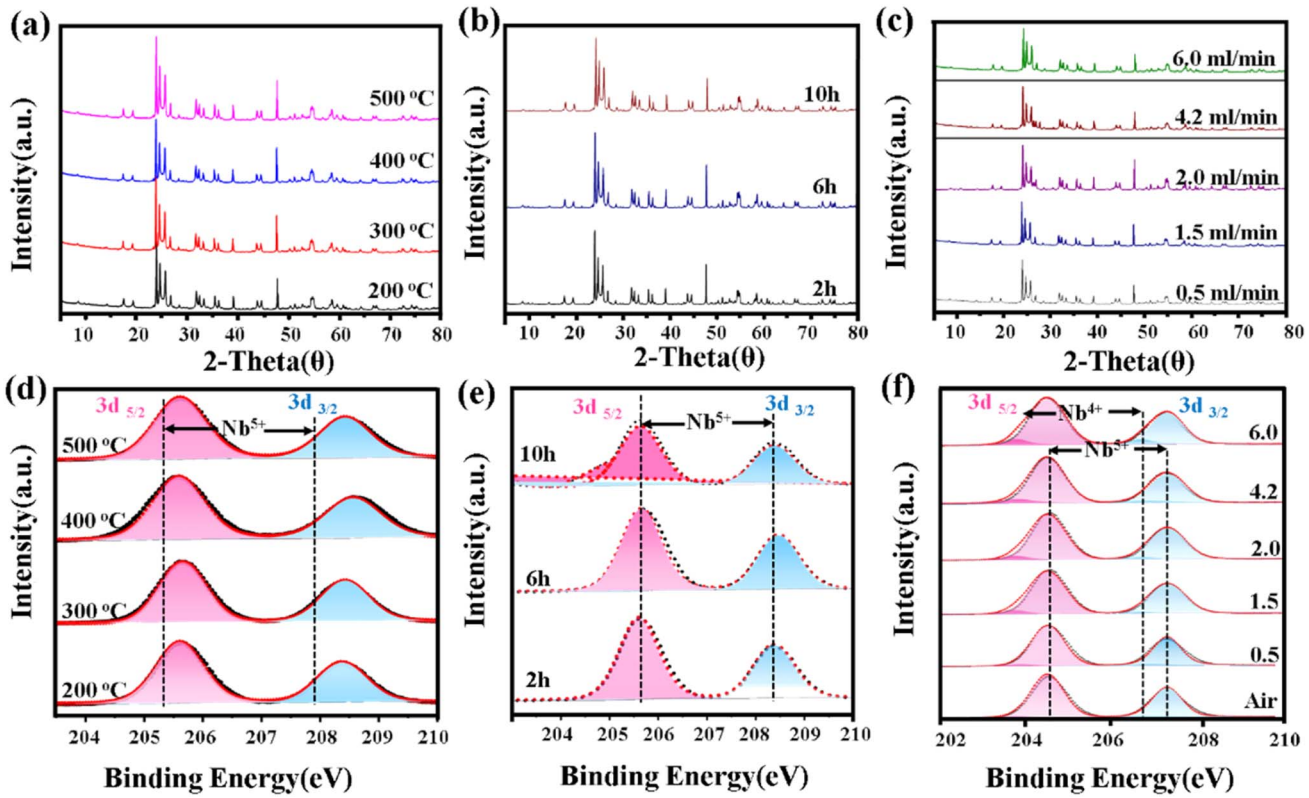

Fig. 7 Effect of temperature (a and d), time (b and e), and NH_3 (c and f) flow rate on the crystalline phases and oxidation states of niobium oxides: XRD and XPS.

flow rate. Furthermore, XPS spectra (Fig. 7f) reveal a shift in the Nb 3d binding energy toward lower values (204.9 eV and 207.8 eV), indicating the coexistence of Nb^{5+} and Nb^{4+} species. Notably, at higher NH_3 flow rates, the Nb^{5+}/Nb^{4+} ratio significantly decreases, suggesting that NH_3 not only facilitates the reduction of Nb_2O_5 but may also lead to the formation of substoichiometric niobium oxides such as NbO_2. This alteration in oxidation state could subsequently influence the electronic structure and catalytic properties of the material.

All experiments were conducted under atmospheric pressure. According to the literature, pressure typically does not significantly impact phase composition in similar reaction systems under ambient conditions. Therefore, the effect of pressure on phase transitions was not explicitly analyzed in this study, as it was not expected to substantially influence the observed results. However, previous studies have reported that in the Nb–O system, pressure can modulate phase stability by altering oxygen vacancy concentration and Nb–O bond length. Specifically, under high-pressure conditions exceeding 1 GPa, Nb_2O_5 may undergo structural rearrangement and transition to NbO_2 or NbO, primarily due to the reduced activation energy for Nb–O bond reconfiguration and oxygen vacancy formation.[61] However, under atmospheric pressure (1 atm), the oxygen vacancy concentration remains relatively low, ensuring the structural stability of Nb_2O_5. Therefore, in the context of this study, we consider the impact of pressure on the phase transition of Nb_2O_5 to be negligible.

To investigate the effect of the Nb^{4+} structure on the acidity of the catalyst, pyridine adsorption infrared spectroscopy (FT-IR) was employed (Fig. 8). Pyridine, used as a probe molecule for acidic sites, allows for differentiation between Brønsted acid sites (B sites) and Lewis acid sites (L sites) based on its characteristic vibrational frequencies when adsorbed. FT-IR analysis was conducted on Nb_2O_5 samples treated with varying NH_3 flow rates, with desorption temperatures of 100 °C, 150 °C, and 350 °C. The results demonstrate a clear increase in the intensity of peaks associated with both B and L acid sites as the NH_3 flow rate increased. Notably, the characteristic L acid peaks at 1450 cm^{-1} and 1600 cm^{-1} became more pronounced, indicating that NH_3 treatment not only facilitated the formation of B acid sites but also significantly enhanced the quantity of L acid sites.[62,63] Additionally, it was observed that the sample treated at an NH_3 flow rate of 2.5 ml min^{-1} exhibited a marked increase in the intensity of the L acid peaks. This detailed analysis highlights the critical role of NH_3 flow rate in modulating the acid properties of Nb_2O_5, with particular emphasis on the enhancement of Lewis acidity, a key factor in catalytic performance.

Fig. 9a presents the O 1s XPS spectra reveal two key oxygen components in Nb_2O_5, lattice oxygen (O_1) and oxygen vacancies (O_2). The detailed O 1s data under different ammonia flow rates are presented in the Fig. S6.† The O_1 component corresponds to highly ordered lattice oxygen atoms bound to niobium, which are stable and exhibit low reactivity.[58] The O_2 component is attributed to oxygen vacancies formed when Nb^{5+} is reduced to Nb^{4+} due to the loss of lattice oxygen. The presence of oxygen vacancies leads to the formation of coordinatively unsaturated metal centers, which are crucial for the catalytic properties of the material. As ammonia flow rate increases, the oxygen vacancy content initially rises, reaching a peak, and then decreases at higher ammonia flow rates due to the loss of surface-adsorbed oxygen. This volcano-shaped trend illustrates that excessive reduction beyond a certain point disrupts the balance of oxygen vacancies, thereby affecting the catalyst's ability to activate reactants.

This relationship between oxygen vacancies and acidic sites is further confirmed by the measurements of Brønsted and Lewis acid sites in Fig. 9b. The optimal number of both B acid and L acid sites is achieved at an ammonia flow rate of 2 ml min^{-1}, where the oxygen vacancy content is maximized. The formation of these vacancies not only reduces Nb^{5+} to Nb^{4+} but also facilitates the generation of a larger number of acidic sites. Brønsted acid sites (B acid) play a crucial role in activating DMA by providing proton transfer pathways, enhancing the reactivity of DMA with ammonia. On the other hand, Lewis acid sites (L acid) assist in the adsorption and activation of electron-donating molecules, promoting the overall reaction.

Raman spectroscopy further reveals the structural impact of ammonia treatment on Nb_2O_5 (Fig. 9c), particularly at a flow rate of 2 ml min^{-1}, where the signal intensity corresponding to Nb–O–Nb bridging and edge sites is significantly enhanced.[64,65] This observation indicates that the strengthening of Nb–O–Nb

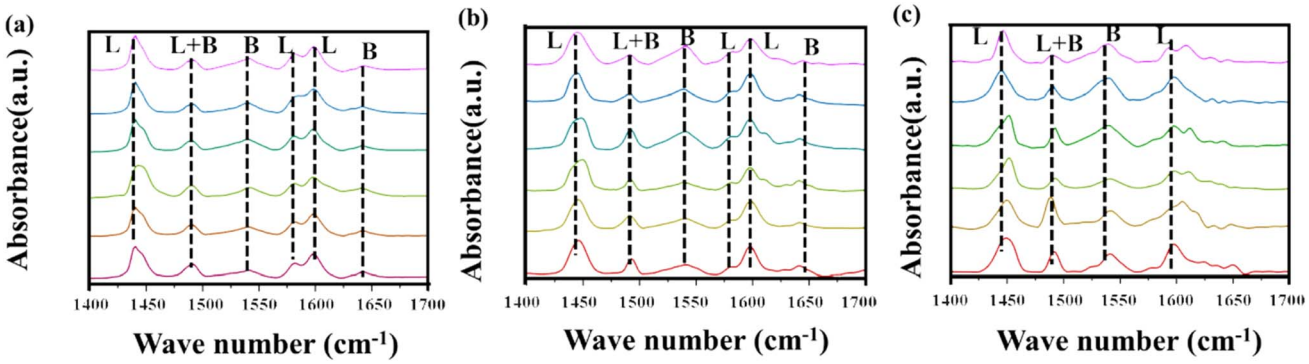

Fig. 8 Infrared spectra of pyridine adsorption at different desorption temperatures after treatment with different ammonia flow rates: (a) 100 °C; (b) 150 °C; (c) 350 °C.

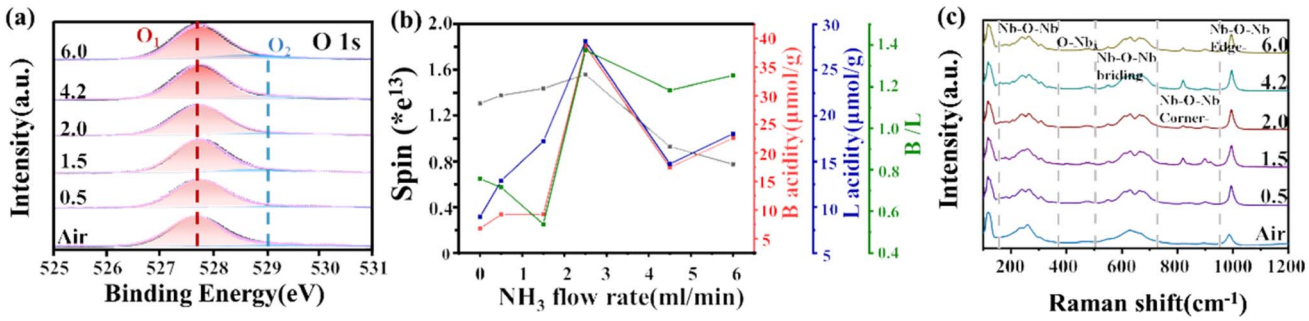

Fig. 9 (a) The O 1s XPS spectra; (b) the different acid amount and the corresponding Ov ratio of the catalysts; and (c) the Raman shift.

bridging bonds and the increase in edge sites under this condition promote the formation of oxygen vacancies.[66] Changes in these bridging and edge sites imply that the reorganization of the Nb_2O_5 surface structure is beneficial for generating active sites, thereby enhancing the adsorption and activation of reactants and ultimately improving catalytic performance. Specifically, the enhancement of Nb–O–Nb bridging and edge sites is closely linked to the increased concentration of B acid sites, as these structural modifications provide more binding sites for protons, thus augmenting the strength and quantity of Brønsted acid sites.[67] This suggests that the structural changes observed in Raman spectra are directly correlated with the formation of B acid sites.

In the reaction of dimethyl adipate with ammonia to form adiponitrile, an excess of B acid sites has a pronounced influence on the reaction mechanism.[68,69] The B acid sites activate dimethyl adipate by providing proton transfer pathways, thereby facilitating its reactivity with ammonia. However, when B acid sites are in excess, the proton transfer reaction can become overly intense, leading to the rapid activation of intermediates and consequently accelerating adiponitrile formation. The acceleration of this reaction pathway is closely related to the formation of oxygen vacancies and the increased concentration of B acid sites. The presence of oxygen vacancies not only increases the number of active sites but also enhances the adsorption and conversion of reactants through the increased influence of surface Brønsted acid sites. Nevertheless, an excess of both B acid and L acid sites may result in side reactions, such as the over-acceleration of adiponitrile formation and rapid carbon deposition, which can cover the catalyst surface and hinder reactant adsorption, ultimately lowering the overall catalytic efficiency. Therefore, it is essential to control an appropriate ammonia-to-ester ratio during the reaction to avoid the side reactions and carbon deposition associated with excessive B and L acid sites.

4. Conclusion

This study systematically investigated the deactivation mechanisms of Nb_2O_5 catalysts in a fixed-bed reactor, revealing that carbon deposition and structural phase transformations are the primary contributors to catalyst deactivation. During the reaction, carbon deposits evolved from monocyclic to polycyclic aromatic hydrocarbons, leading to the blockage of critical acid sites and diminished catalytic activity. Simultaneously, Nb_2O_5 underwent a phase transformation to $Nb_{12}O_{29}$, and catalyst regeneration partially reversed this transformation, restoring Nb_2O_5 content and reducing $Nb_{12}O_{29}$. This phase change facilitated the formation of oxygen vacancies, which created unsaturated metal coordination sites, altering the catalyst's acidity profile. The findings emphasize the importance of maintaining moderate acidity to achieve efficient conversion and high nitrile selectivity. Additionally, strategies to mitigate coke formation and stabilize active catalyst sites are essential for improving the stability, reusability, and overall performance of Nb_2O_5 catalysts.

Building on these findings, the study also highlights the practical implications for large-scale industrial applications. The stability and reusability of catalysts are crucial for optimizing industrial production, particularly in the manufacture of nitrile-based chemicals. This research provides a theoretical basis for improving catalyst stability, reducing energy consumption, and extending catalyst lifetime. By optimizing ammonia flow rates and controlling acidic sites, future research can enhance catalytic efficiency and minimize maintenance costs, thus contributing to more efficient and sustainable industrial processes.

Data availability

The data supporting this article have been included within the manuscript and its ESI.†

Conflicts of interest

The authors declare no competing financial interest.

Acknowledgements

This work was financially funded by the National Key R&D Program of China (2022YFA1504902), National Natural Science Foundation of China (No. 22178358, 22078337, 22078336), the Young Scientists Fund of the National Natural Science Foundation of China (No. 22408376), the Postdoctoral Fellowship Program of CPSF (GZC20232700) and the "Special Research Assistant Project" of the Chinese Academy of Sciences.

References

1 K. Geng, H. Li, D. Zhang, B. Yu, H. Hu, J. Geng, Y. Wu and X. Hu, Producing hexamethylenediamine from caprolactam *via* 6-aminocapronitrile: a green production technology of the monomer of nylon-66, *Green Chem.*, 2024, 8777–8784, DOI: 10.1039/d4gc02268h.

2 R. Beerthuis, G. Rothenberg and N. R. Shiju, Catalytic routes towards acrylic acid, adipic acid and ε-caprolactam starting from biorenewables, *Green Chem.*, 2015, **17**(3), 1341–1361, DOI: 10.1039/c4gc02076f.

3 W. C. Drinkard and R. V. Lind sey Jr, Hydrocyanation of olefins using selected nickel phosphite catalysts, *US Pat.*, 1970.

4 J. Yang, P. Wang, H. Neumann, R. Jackstell and M. Beller, Industrially applied and relevant transformations of 1,3-butadiene using homogeneous catalysts, *Ind. Chem. Mater.*, 2023, **1**(2), 155–174, DOI: 10.1039/d3im00009e.

5 M. M. Baizer and J. L. Chruma, Electrolytic Reductive Coupling: XX. Mixed Reductive Couplings with Acrylonitrile Reductions at the Cathode Voltage Required for the More Difficultly Reduced Partner, *J. Electrochem. Soc.*, 1971, **118**, 3, DOI: 10.1149/1.2408079.

6 M. Seko, K. Mihara, S. Kumazaki, R. Komori and M. Yoshida, Adiponitrile production by the electrolytic hydrodimerization of acrylonitrile, *US Pat.*, US3595764, 1971.

7 A. S. Nizami, X. Luo, J. Dou, A. Bai, L. Wang, M. Wei, M. J. K. Bashir and H. Ganjidoust, Production technology of adiponitrile, *E3S Web Conf.*, 2023, **441**, 01019, DOI: 10.1051/e3sconf/202344101019.

8 L. Du, Z.-T. Cao, X.-M. Wang, M.-Q. Wang, B.-C. Sun, G.-W. Chu and J.-F. Chen, Reaction kinetics and mechanism of adiponitrile preparation by adipic acid ammoniation, *Chem. Eng. Sci.*, 2024, **290**, 119851, DOI: 10.1016/j.ces.2024.119851.

9 H. Zhao, H. Wei, Y. Guo, L. Han, L. Wang, Y. Hu and J. Xin, Study on the stability of palladium complexes with Hemaraphos ligand and reaction kinetics in the bis-hydroalkoxycarbonylation of 1,3-butadiene, *J. Catal.*, 2023, **428**, 115160, DOI: 10.1016/j.jcat.2023.115160.

10 L. Wang, Z. Zhao, S. Wang, W. Zhou, X. Lu, R. Yan and J. Xin, Unveiling the hydroesterification of 1,3-butadiene with carbonyl cobalt ionic liquids: Facilitation of cationic protonic hydrogen for active species formation, *J. Catal.*, 2024, **434**, 115525, DOI: 10.1016/j.jcat.2024.115525.

11 T. Guo, F.-Y. Yan, Y.-F. Wang, X.-F. Xu, Q.-Z. Jia and B.-H. Xu, Boosted nitrilation of dimethyl adipate with NH3 to adiponitrile over bimetallic oxide: Synergetic effect between Nb and W, *Chem. Eng. Sci.*, 2023, **281**, 119121, DOI: 10.1016/j.ces.2023.119121.

12 Z. H. Zhang, L. J. Han, S. S. Ma, Y. R. Du, Z. K. Yu, J. Q. Lin and B. H. Xu, Scalable Palladium-Catalyzed Alkoxycarbonylation of Conjugated Dienes, *J. Org. Chem.*, 2023, **88**(2), 882–892, DOI: 10.1021/acs.joc.2c02245.

13 G.-R. Ding, Y.-F. Wang, G.-Y. Duan, T. Guo, X.-F. Xu, C.-S. Li and B.-H. Xu, Chemoselective nitrilation of dimethyl adipate with ammonia over carbon encapsulated WOx catalysts under continuous flow conditions, *Catal. Sci. Technol.*, 2022, **12**(12), 3982–3991, DOI: 10.1039/d2cy00733a.

14 Y. Shirazi, H. Tafazolian, S. Viamajala, S. Varanasi, Z. Song and M. J. Heben, High-Yield Production of Fatty Nitriles by One-Step Vapor-Phase Thermocatalysis of Triglycerides, *ACS Omega*, 2017, **2**(12), 9013–9020, DOI: 10.1021/acsomega.7b01502.

15 M. Eric, T. R. E. Karp, V. Sànchez i Nogué, V. Vorotnikov, M. J. Biddy, E. C. D. Tan, D. G. Brandner, R. M. Cywar, R. Liu, L. P. Manker, W. E. Michener, M. Gilhespy, Z. Skoufa, M. J. Watson, O. Stanley Fruchey, D. R. Vardon, R. T. Gill, A. D. Bratis and G. T. Beckham, Renewable acrylonitrile production, *Science*, 2017, **358**(6368), 1307–1310.

16 A. Mekki-Berrada, S. Bennici, J. P. Gillet, J. L. Couturier, J. L. Dubois and A. Auroux, Ammoniation-dehydration of fatty acids into nitriles: heterogeneous or homogeneous catalysis?, *ChemSusChem*, 2013, **6**(8), 1478–1489, DOI: 10.1002/cssc.201300210.

17 A. Mekki-Berrada, S. Bennici, J. P. Gillet, J. L. Couturier, J. L. Dubois and A. Auroux, Fatty acid methyl esters into nitriles: Acid–base properties for enhanced catalysts, *J. Catal.*, 2013, **306**, 30–37, DOI: 10.1016/j.jcat.2013.05.032.

18 X.-F. Xu, Y.-F. Wang, T. Guo, L.-K. Luan, S.-S. Liu and B.-H. Xu, Synthesis of adiponitrile from dimethyl adipate and ammonia in the vapor-phase over niobium oxide, *Catal. Sci. Technol.*, 2022, **12**(12), 3947–3956, DOI: 10.1039/d2cy00734g.

19 U. E. Amjad, A. Tajjamal, A. Ul-Hamid, A. Faisal, S. A. H. Zaidi, L. Sherin, A. Mir, M. Mustafa, N. Ahmad, M. Hussain, *et al.*, Catalytic cracking of polystyrene pyrolysis oil: effect of $Nb_{(2)}O_{(5)}$ and $NiO/Nb_{(2)}O_{(5)}$ catalyst on the liquid product composition, *Waste Manage.*, 2022, **141**, 240–250, DOI: 10.1016/j.wasman.2022.02.002.

20 Y. Li, J. Guo, H. Liu, A. Liu and D. Li, *In situ generated oxygen vacancy on Nb_2O_5 for boosted catalytic activities of M/Nb_2O_5 in photothermal CO_2 reforming of CH_4 J. CO2 Util.*, 2023, **67**, 102330, DOI: 10.1016/j.jcou.2022.102330.

21 H. L. Kaiyi Su, Z. Gao, P. Fornasiero and F. Wang, Nb_2O_5-Based Photocatalysts, *Adv. Sci.*, 2021, 2003156, DOI: 10.1002/advs.202003156.

22 C. H. Bartholomew, Mechanisms of catalyst deactivation, *Appl. Catal., A*, 2001, **212**, 17–60.

23 T. Z. Bo Yuan, Y. Han, X. Zhang, M. Wang and Li Chen, Deactivation Mechanism and Anti-Deactivation Measures of Metal Catalyst in the Dry Reforming of Methane: A Review, *Atmosphere*, 2023, **14**(5), 770, DOI: 10.3390/atmos14050770.

24 F. Pio and L. Luca, Catalyst deactivation, *Catal. Today*, 1999, **52**(2–3), 165–181.

25 M. Argyle and C. Bartholomew, Heterogeneous Catalyst Deactivation and Regeneration: A Review, *Catalysts*, 2015, **5**(1), 145–269, DOI: 10.3390/catal5010145.

26 Z. Chen, Y. Ye, X. Feng, Y. Wang, X. Han, Y. Zhu, S. Wu, S. Wang, W. Yang, L. Wang, *et al.*, High-density frustrated Lewis pairs based on Lamellar $Nb_{(2)}O_{(5)}$ for photocatalytic

non-oxidative methane coupling, *Nat. Commun.*, 2023, **14**(1), 2000, DOI: 10.1038/s41467-023-37663-x.

27 R. Pang, Z. Wang, J. Li and K. Chen, Polymorphs of $Nb_{(2)}O_{(5)}$ Compound and Their Electrical Energy Storage Applications, *Materials*, 2023, **16**(21), 6956, DOI: 10.3390/ma16216956.

28 V. G. F. Pereira, C. R. Moreira, C. P. Rodrigues and F. S. Toniolo, Influence of active sites and the reaction conditions on the ethanol upgrading over Nb_2O_5/ZrO_2 based multifunctional catalysts, *Braz. J. Chem. Eng.*, 2022, **40**(4), 1039–1054, DOI: 10.1007/s43153-022-00287-7.

29 J. Li, G. Lu, K. Li and W. Wang, Active Nb_2O_5-supported nickel and nickel–copper catalysts for methane decomposition to hydrogen and filamentous carbon, *J. Mol. Catal. A: Chem.*, 2004, **221**(1–2), 105–112, DOI: 10.1016/j.molcata.2004.06.015.

30 G. R. Ding, Y. F. Wang, G. Y. Duan, Y. Q. Fan and B. H. Xu, Adjustment of W-O-Zr Boundaries Boosts Efficient Nitrilation of Dimethyl Adipate with Ammonia on $WO_{(x)}/ZrO_{(2)}$ Catalysts, *ACS Appl. Mater. Interfaces*, 2023, **15**(2), 3633–3643, DOI: 10.1021/acsami.2c18908.

31 L. Yan, Y. Liu, K. Zha, H. Li, L. Shi and D. Zhang, Deep insight into the structure–activity relationship of Nb modified SnO_2–CeO_2 catalysts for low-temperature selective catalytic reduction of NO by NH_3, *Catal. Sci. Technol.*, 2017, 7(2), 502–514, DOI: 10.1039/c6cy02242a.

32 Y. Li, C. Zhang, Y. Liu, X. Hou, R. Zhang and X. Tang, Coke Deposition on Ni/HZSM-5 in Bio-oil Hydrodeoxygenation Processing, *Energy Fuels*, 2015, **29**(3), 1722–1728, DOI: 10.1021/ef5024669.

33 M. J. Wulfers and F. C. Jentoft, Identification of carbonaceous deposits formed on H-mordenite during alkane isomerization, *J. Catal.*, 2013, **307**, 204–213, DOI: 10.1016/j.jcat.2013.07.011.

34 X.-Y. Ren, J.-P. Cao, S.-X. Zhao, X.-Y. Zhao, X.-B. Feng, T.-L. Liu, Y. Li, J. Zhang and X.-Y. Wei, Insights into coke location of catalyst deactivation during in-situ catalytic reforming of lignite pyrolysis volatiles over cobalt-modified zeolites, *Appl. Catal., A*, 2021, **613**, 118018, DOI: 10.1016/j.apcata.2021.118018.

35 P. Magnoux, C. Canaff, F. Machado and M. Guisnet, Coking, Aging, and Regeneration of Zeolites, *J. Catal.*, 1992, **134**, 286–298.

36 L. Y. Jia, A. Farouha, L. Pinard, S. Hedan, J. D. Comparot, A. Dufour, K. Ben Tayeb, H. Vezin and C. Batiot-Dupeyrat, New routes for complete regeneration of coked zeolite, *Appl. Catal., B*, 2017, **219**, 82–91, DOI: 10.1016/j.apcatb.2017.07.040.

37 M. Díaz, E. Epelde, J. Valecillos, S. Izaddoust, A. T. Aguayo and J. Bilbao, Coke deactivation and regeneration of HZSM-5 zeolite catalysts in the oligomerization of 1-butene, *Appl. Catal., B*, 2021, **291**, 120076, DOI: 10.1016/j.apcatb.2021.120076.

38 L. Palumbo, F. Bonino, P. Beato, M. Bjørgen and A. Zecchina, Conversion of methanol to hydrocarbons: spectroscopic characterization of carbonaceous species formed over H-ZSM-5, *J. Phys. Chem. C*, 2008, **112**(26), 9710–9716.

39 P. Rzepka, D. Sheptyakov, C. Wang, J. A. van Bokhoven and V. Paunović, How Micropore Topology Influences the Structure and Location of Coke in Zeolite Catalysts, *ACS Catal.*, 2024, **14**(8), 5593–5604, DOI: 10.1021/acscatal.4c00025.

40 F. F. Madeira, H. Vezin, N. S. Gnep, P. Magnoux, S. Maury and N. Cadran, Radical Species Detection and Their Nature Evolution with Catalyst Deactivation in the Ethanol-to-Hydrocarbon Reaction over HZSM-5 Zeolite, *ACS Catal.*, 2011, **1**(4), 417–424, DOI: 10.1021/cs2000686.

41 L. K. Shrestha, L. Adhikari, R. G. Shrestha, M. P. Adhikari, R. Adhikari, J. P. Hill, R. R. Pradhananga and K. Ariga, Nanoporous carbon materials with enhanced supercapacitance performance and non-aromatic chemical sensing with C(1)/C(2) alcohol discrimination, *Sci. Technol. Adv. Mater.*, 2016, **17**(1), 483–492, DOI: 10.1080/14686996.2016.1219971.

42 H. V. Lin, D. S. Chan, Y. H. Huang and W. C. Sung, Kinetics of Moisture Loss and Oil Absorption of Pork Rinds during Deep-Fat, Microwave-Assisted and Vacuum Frying, *Foods*, 2021, **10**(12), 3025, DOI: 10.3390/foods10123025.

43 A. C. Ferrari, Raman spectroscopy of graphene and graphite: Disorder, electron–phonon coupling, doping and nonadiabatic effects, *Solid State Commun.*, 2007, **143**(1–2), 47–57, DOI: 10.1016/j.ssc.2007.03.052.

44 I Childres, L. A. Jauregui and Y. P. Chen, Raman spectra and electron-phonon coupling in disordered graphene with gate-tunable doping, *J. Appl. Phys.*, 2014, **22**, 243–250.

45 Z. Cheng, S. Huang, Y. Li, K. Cai, D. Yao, J. Lv, S. Wang and X. Ma, Carbonylation of dimethyl ether over MOR and Cu/H-MOR catalysts: Comparative investigation of deactivation behavior, *Appl. Catal., A*, 2019, **576**, 1–10, DOI: 10.1016/j.apcata.2019.02.032.

46 X. Xian, C. Ran, C. Nai, P. Yang, S. Zhao and L. Dong, Characterization of the location of coke deposited on spent HZSM-5 zeolite by special temperature-programmed oxidation and isothermal oxidation methods, *Appl. Catal., A*, 2017, **547**, 37–51, DOI: 10.1016/j.apcata.2017.08.023.

47 T. Vazhnova, S. P. Rigby and D. B. Lukyanov, Benzene alkylation with ethane in ethylbenzene over a PtH-MFI catalyst: Kinetic and IR investigation of the catalyst deactivation, *J. Catal.*, 2013, **301**, 125–133, DOI: 10.1016/j.jcat.2013.02.002.

48 C. Song, K. Liu, D. Zhang, S. Liu, X. Li, S. Xie and L. Xu, Effect of cofeeding n-butane with methanol on aromatization performance and coke formation over a Zn loaded ZSM-5/ZSM-11 zeolite, *Appl. Catal., A*, 2014, **470**, 15–23, DOI: 10.1016/j.apcata.2013.10.036.

49 X.-G. Li, X. Huang, Y.-L. Zhang, H. Li, W.-D. Xiao and Z. Wei, Effect of n-butanol cofeeding on the deactivation of methanol to olefin conversion over high-silica HZSM-5: A mechanism and kinetic study, *Chem. Eng. Sci.*, 2020, **226**, 115859, DOI: 10.1016/j.ces.2020.115859.

50 T. Cordero-Lanzac, A. Ateka, P. Pérez-Uriarte, P. Castaño, A. T. Aguayo and J. Bilbao, Insight into the Deactivation and Regeneration of HZSM-5 Zeolite Catalysts in the Conversion of Dimethyl Ether to Olefins, *Ind. Eng. Chem.*

Res., 2018, **57**(41), 13689–13702, DOI: **10.1021/acs.iecr.8b03308**.

51 X. Huang, X. Jiao, M. Lin, K. Wang, L. Jia, B. Hou and D. Li, Coke distribution determines the lifespan of a hollow Mo/HZSM-5 capsule catalyst in CH4 dehydroaromatization, *Catal. Sci. Technol.*, 2018, **8**(22), 5740–5749, DOI: **10.1039/c8cy01391h**.

52 H. Xu, Z. Wang, Z. Miao, Y. Zhu, A. Marianov, L. Wang, P. Castignolles, M. Gaborieau, J. Huang and Y. Jiang, Correlation between Acidity and Catalytic Performance of Mesoporous Zirconium Oxophosphate in Phenylglyoxal Conversion, *ACS Sustain. Chem. Eng.*, 2019, **7**(9), 8931–8942, DOI: **10.1021/acssuschemeng.9b00989**.

53 H. T. Kreissl, K. Nakagawa, Y.-K. Peng, Y. Koito, J. Zheng and S. C. E. Tsang, Niobium oxides: Correlation of acidity with structure and catalytic performance in sucrose conversion to 5-hydroxymethylfurfural, *J. Catal.*, 2016, **338**, 329–339, DOI: **10.1016/j.jcat.2016.03.007**.

54 M. Chakraborty and H.-J. Bart, Highly selective and efficient transport of toluene in bulk ionic liquid membranes containing Ag^+ as carrier, *Fuel Process. Technol.*, 2007, **88**(1), 43–49, DOI: **10.1016/j.fuproc.2006.08.004**.

55 V. V. Atuchin, I. E. Kalabin, V. G. Kesler and N. V. Pervukhina, Nb 3d and O 1s core levels and chemical bonding in niobates, *J. Electron Spectrosc. Relat. Phenom.*, 2005, **142**(2), 129–134, DOI: **10.1016/j.elspec.2004.10.003**.

56 Z. Zhang, H. Xu and H. Li, Insights into the catalytic performance of Ni/Nb_2O_5 catalysts for vanillin hydrodeoxygenation in aqueous phase: the role of Nb_2O_5 crystal structures, *Fuel*, 2022, **324**, 124400, DOI: **10.1016/j.fuel.2022.124400**.

57 Z. Weibin, W. Weidong, W. Xueming, C. Xinlu, Y. Dawei, S. Changle, P. Liping, W. Yuying and B. Li, The investigation of NbO_2 and Nb_2O_5 electronic structure by XPS, UPS and first principles methods, *Surf. Interface Anal.*, 2013, **45**(8), 1206–1210, DOI: **10.1002/sia.5253**.

58 Y. Zou, Y. Hu, A. Uhrich, Z. Shen, B. Peng, Z. Ji, M. Muhler, G. Zhao, X. Wang and X. Xu, Steering accessible oxygen vacancies for alcohol oxidation over defective Nb_2O_5 under visible light illumination, *Appl. Catal., B*, 2021, **298**, 120584, DOI: **10.1016/j.apcatb.2021.120584**.

59 A. Barrera, J. A. Montoya, M. Viniegra, J. Navarrete, G. Espinosa, A. Vargas, P. del Angel and G. Pérez, Isomerization of n-hexane over mono- and bimetallic Pd–Pt catalysts supported on ZrO_2–Al_2O_3–WO_x prepared by sol–gel, *Appl. Catal., A*, 2005, **290**(1–2), 97–109, DOI: **10.1016/j.apcata.2005.05.011**.

60 L. Sun, J. Sun, S. Zhai, H. Yang, X. Chen, W. Q. Deng and H. Wu, Nb(2) CT(x) MXene Derived Polymorphic $Nb_{(2)}O_{(5)}$, *Small*, 2023, **19**(26), e2300914, DOI: **10.1002/smll.202300914**.

61 Z. Guan, Q. Li, H. Zhang, P. Shen, L. Zheng, S. Chu, C. Park, X. Hong, R. Liu, P. Wang, *et al.*, Pressure induced transformation and subsequent amorphization of monoclinic $Nb_{(2)}O_{(5)}$ and its effect on optical properties, *J. Phys.:Condens. Matter*, 2019, **31**(10), 105401, DOI: **10.1088/1361-648X/aaf9bd**.

62 K. Stawicka, P. Decyk, A. Wojtaszek-Gurdak and M. Ziolek, Comparative study of acid-basic properties of MCF impregnated with niobium and cerium species, *Catal. Today*, 2019, **325**, 2–10, DOI: **10.1016/j.cattod.2018.05.025**.

63 C. A. Emeis, Determination of Integrated Molar Extinction Coefficients for Infrared Absorption Bands of Pyridine Adsorbed on Solid Acid Catalysts, *J. Catal.*, 1993, **141**, 347–354.

64 S. M. A. H. Siddiki, M. N. Rashed, A. S. Touchy, M. A. R. Jamil, Y. Jing, T. Toyao, Z. Maeno and K.-i. Shimizu, Hydrolysis of amides to carboxylic acids catalyzed by Nb_2O_5, *Catal. Sci. Technol.*, 2021, **11**(5), 1949–1960, DOI: **10.1039/d0cy02230f**.

65 T. Ikeya and M. Senna, Change in the structure of ninbium pentoxide due to mechanical and thermal treatments, *J. Non-Cryst. Solids*, 1988, **105**, 243–250.

66 G. D. Wilk, R. M. Wallace and J. M. Anthony, High-κ gate dielectrics: current status and materials properties considerations, *J. Appl. Phys.*, 2001, **89**, 5243–5275, DOI: **10.1063/1.1361065**.

67 U. Balachandran and N. G. Eror, Raman spectrum of the high temperature form of Nb_2O_5, *J. Mater. Sci. Lett.*, 1982, 374–376.

68 M. A. Ali, S. M. A. H. Siddiki, W. Onodera, K. Kon and K. i. Shimizu, Amidation of Carboxylic Acids with Amines by Nb_2O_5 as a Reusable Lewis Acid Catalyst, *ChemCatChem*, 2015, **7**(21), 3555–3561, DOI: **10.1002/cctc.201500672**.

69 M. A. Ali, S. K. Moromi, A. S. Touchy and K. i. Shimizu, Direct Synthesis of Cyclic Imides from Carboxylic Anhydrides and Amines by Nb_2O_5 as a Water-Tolerant Lewis Acid Catalyst, *ChemCatChem*, 2016, **8**(5), 891–894, DOI: **10.1002/cctc.201501172**.